Testing coalescence and statistical-thermal production scenarios for (anti-)(hyper-)nuclei and exotic QCD objects at LHC energies

Francesca Bellini* and Alexander P. Kalweit†

European Organization for Nuclear Research (CERN),
Geneva, Switzerland

(Dated: September 24, 2018)

We present a detailed comparison of coalescence and thermal-statistical models for the production of (anti-)(hyper-)nuclei in high-energy collisions. For the first time, such a study is carried out as a function of the size of the object relative to the size of the particle emitting source. Our study reveals large differences between the two scenarios for the production of objects with extended wave-functions. While both models give similar predictions and show similar agreement with experimental data for (anti-)deuterons and (anti-)^{3}He nuclei, they largely differ in their description of (anti-)hyper-triton production. We propose to address experimentally the comparison of the production models by measuring the coalescence parameter systematically for different (anti-)(hyper-)nuclei in different collision systems and differentially in multiplicity. Such measurements are feasible with the current and upgraded LHC experiments. Our findings highlight the unique potential of ultra-relativistic heavy-ion collisions as a laboratory to clarify the internal structure of exotic QCD objects and can serve as a basis for more refined calculations in the future.

I. INTRODUCTION

The formation of light anti- and hyper-nuclei in high energy proton-proton (pp), proton-nucleus (pA) and nucleus-nucleus (AA) collisions provides unique observables for the study of the system created in these collisions. In addition, these studies might shed light on the internal structure of the formed objects themselves. Nuclei and hyper-nuclei are special objects with respect to non-composite hadrons (such as pions, kaons, protons, etc.), because their size (i.e. the extension of their wave-function) is comparable to a fraction or the whole system created in the collision [1]. The relevant known properties of the objects under study here are summarised in Tab. I. As quantum-mechanical objects, their size is typically defined as the rms of their (charge) wave-function, which corresponds to about 2 fm for light (anti-)nuclei as obtained from electron scattering experiments. For the hyper-triton, theoretical calculations indicate a rms of the wave-function of about 5 fm [2], which is significantly larger than that of non-strange nuclei with mass number $A = 3$. This is driven by the average separation of the Λ with respect to the two other nucleons which is expected to amount to up to 10 fm [2].

Since about sixty years, coalescence models have been used to describe the formation of composite objects (see for instance [3–11] and references therein). Surprisingly, thermal-statistical models have been successful in describing not only light-flavour particle production, but also that of light (anti-)(hyper-)nuclei across a wide range of energies in nucleus-nucleus collisions [12, 13]. In this approach, particles are produced from a fireball in thermal and kinetic equilibrium with temperatures of the or-

der of $T_{chem} \approx 156$ MeV that are near the temperature of the QCD phase transition boundary, as predicted by lattice QCD calculations [14, 15]. Particle abundances are fixed at chemical freeze-out, when inelastic collisions cease. Further elastic and pseudo-elastic collisions occur among the components of the expanding fireball, that can affect the spectral shapes and the measurable yields of short-lived (strongly decaying) hadronic resonances. Once the particle density of the system is so low that the mean free path for elastic collisions is larger than the size of the system, the fireball freezes-out kinetically at temperatures of the order of $T_{kin} \approx 90$ MeV [16]. In such a dense and hot environment, composite objects with binding energies that are small with respect to the temperature of the system, appear as "fragile" objects. For instance, the binding energy of the deuteron is $B_{E,d} = 2.2$ MeV $\ll T_{chem}, T_{kin}$. As a matter of fact, the cross-section for pion-induced deuteron breakup is significantly larger than the typical (pseudo)-elastic cross-sections for the re-scattering of hadronic resonance decay products [17–19]. Similarly, the elastic cross-section which drives the deuteron spectra to kinetic equilibration in central heavy-ion collisions [20] is smaller than the breakup cross-section [17–19]. Based on this, the deuterons produced at chemical freeze-out would be expected not to survive the hadronic phase of the medium expansion, yet their production is measured to be consistent to the predictions from statistical-thermal models and they develop also a non-zero elliptic flow which is consistent with a common radial expansion together with the non-composite hadrons [20]. Several solutions have been proposed to solve this "light (anti-)nuclei puzzle": (a.) a sudden freeze-out at the QGP-hadron phase boundary, (b.) the thermal production of these objects as compact quark bags [12], and (c.) the coincidence of the coalescence mechanism with that of thermal production [7, 21]. Data from rescattering of short-lived hadronic resonances in-

Mass number	Nucleus	Composition	B_E (MeV)	J_A	$\lambda_A{}^{meas}$ (fm)	r_A (fm)	Refs.
A = 2	d	pn	2.224575 (9)	1	2.1413 ± 0.0025	3.2	[23, 24]
A = 3	^{3}H	pnn	8.4817986 (20)	1/2	1.755 ± 0.086	2.15	[25]
	^{3}He	ppn	7.7180428 (23)	1/2	1.959 ± 0.030	2.48	[25]
	${}^3_\Lambda$H	pΛn	0.13 ± 0.05	1/2	$4.9 - 10.0$	$6.8 - 14.1$	[2, 26]
A = 4	^{4}He	ppnn	28.29566 (20)	0	1.6755 ± 0.0028	1.9	[27, 28]
	${}^4_\Lambda$H	pΛnn	2.04 ± 0.04	0	$2.0 - 3.8$	$2.4 - 4.9$	[2, 26]
	${}^4_{\Lambda\Lambda}$H	pΛΛn	$0.39 - 0.51$	1	$4.2 - 7.1$	$5.5 - 9.4$	[2]
	${}^4_\Lambda$He	ppΛn	2.39 ± 0.03	0	$2.0 - 3.8$	$2.4 - 4.9$	[2, 26]

TABLE I. Properties of nuclei and hyper-nuclei with mass number $A \leq 4$. B_E is the binding energy in MeV, J_A is the spin. The size of the nucleus is given in terms of the (charge) rms radius of the wave-function, λ_A. The size parameter of the wave-function of the harmonic oscillator potential, r_A, is chosen such that the measured/expected rms, $\lambda_A{}^{meas}$ (fm), is approximately reproduced. Details are given in Appendix A. Please note that the proton rms charge radius $\lambda_p = 0.879(8)$ fm [29] is subtracted quadratically from the measured rms charge radius λ_A^{meas} of the nucleus $\lambda_A = \sqrt{(\lambda_A^{meas})^2 - \lambda_p^2}$ to account for the finite extension of the constituents. Implicitly we assume here that $\lambda_\Lambda \approx \lambda_n \approx \lambda_p$. References are given in the last column. The spin of ${}^4_{\Lambda\Lambda}$H is discussed in the text of [2].

dicate that the system undergoes a long-lasting hadronic phase before decoupling [22], thus strongly disfavouring hypothesis (a.). While hypothesis (b.) cannot presently be tested beyond the agreement of measured (anti-)nuclei production yields with statistical-thermal model predictions, hypothesis (c.) is scrutinised in the present work.

To this purpose, we compare to models the existing data from the LHC. For the first time, these data allow for the systematic study of the light (anti-)(hyper-)nuclei production as a function of the system and object size. In the nucleon-coalescence approach, nuclei are formed at kinetic freeze-out by coalescence of nucleons that are nearby in space and have similar velocities. The coalescence model is reviewed in Section II, starting from its simplest form (uncorrelated nucleon emission from a point-like source) to the full space-time evolution picture as discussed in [7]. In Section III, a blast-wave parameterisation for particle transverse momentum spectra in combination with predictions from the statistical-thermal model for the yields is used as an alternative approach. The direct comparison of the two approaches and the comparison with data are discussed in Section IV. We find that a systematic study of the coalescence parameter B_A provides an important discrimination power between the two approaches.

A quantitative direct comparison of the two production scenarios has been proposed recently in [30], that resulted in the proposal to study the production rates of nuclei with similar mass but very different internal structure, in particular of ^{4}He and ^{4}Li [10]. However, as the ^{4}Li is not stable with respect to strong decay, its measurement is experimentally very challenging and probably less constraining than the comparison with the hyper-nuclei proposed here. We propose that B_A is systematically measured in all collision systems by exploiting the large statistics sample that will be available with the LHC Run 3 & 4, in order to rule out or support the aforementioned scenarios.

II. COALESCENCE APPROACH

In the coalescence picture, nucleons produced in the collision coalesce into nuclei if they are close in space and have similar velocities [3, 4]. For a nucleus with mass number $A = Z + N$, the coalescence probability is typically quantified in terms of the coalescence parameter B_A. Considering that in the LHC collision energy regime the number of produced protons and neutrons at midrapidity is expected to be equal, B_A is defined as

$$E_A \frac{\mathrm{d}^3 N_A}{\mathrm{d}p_A^3} = B_A \left(E_{\mathrm{p,n}} \frac{\mathrm{d}^3 N_{\mathrm{p,n}}}{\mathrm{d}p_{\mathrm{p,n}}^3} \right)^A \bigg|_{\vec{p}_{\mathrm{p}} = \vec{p}_{\mathrm{n}} = \frac{\vec{p}_A}{A}} . \quad (1)$$

where $p_{\mathrm{p,n}}$ are the momenta of the proton and neutron and $E_{p,n}$ their energies.

Moreover, the LHC is particularly suited for the production of anti-nuclei, since the number of baryons and anti-baryons is essentially equal at midrapidity [36]. As a consequence, also the anti-particle to particle ratio for the light (hyper-)nuclei considered in this work is measured to be consistent with unity in pp, p–Pb and Pb–Pb collisions [20, 37–39]. In a simple coalescence approach, the coalescence parameter is expected to be independent of p_T and of the object size with respect to the volume of particle emission (hereafter referred to as "source volume" or "source size"). In this naive expectation, the number of nuclei produced by coalescence increases with increasing number of nucleons produced in the collision. If the nucleon number increases with the event multiplicity, so does the number of (anti-)nuclei. While this picture is found to be approximately valid in pp and p–Pb collisions [37, 38], it breaks down in Pb–Pb collisions, that exhibit a strong decrease of B_A with centrality [40]. In addition, the elliptic flow of deuterons cannot be explained by simple coalescence [20].

More advanced coalescence models take into account

the size of the particle emission source, as the coalescence probability naturally decreases for two nucleons with similar momenta that are produced far apart in configuration space. While there are several approaches to address this effect [5, 6], in our study we rely on the formalism proposed in [7]. As coalescence is a quantum-mechanical process, the classical definition of phase space is replaced by the Wigner formalism. Therefore, the production probability of a nucleon cluster is given by the overlap of the Wigner function of its internal wave-function with the phase-space distributions of the constituent particles.

The wave-functions of the objects under study are approximated by the ground-state wave-functions of an isotropic spherical harmonic oscillator as in [7] with one single characteristic-size parameter, r_A. For the deuteron ($A = 2$) wave-function $\varphi_d(\vec{r})$, one obtains

$$\varphi_d(\vec{r}) = (\pi r_d^2)^{-3/4} \exp\left(-\frac{r^2}{2r_d^2}\right) . \tag{2}$$

For nuclei with $A > 2$, analogous forms exist (see Appendix A and A for details). The relation between the characteristic size parameter r_A and the rms of the wave-function was derived in [41] as

$$\lambda_A^2 = \frac{3}{2}\frac{A-1}{A}\frac{r_A^2}{2} \tag{3}$$

for point-like constituents. In particular, we obtain $r_d = \sqrt{8/3}\lambda_2$ for $A = 2$, $r_3 = \sqrt{2}\lambda_3$ for $A = 3$, and $r_4 = \sqrt{16/9}\lambda_4$ for $A = 4$ (see Appendix A and A for details).

In this work, we follow the gaussian ansatz in order to obtain fully analytic solutions that highlight the sensitivity to the size of the source (i.e. the centrality dependence) and to the size of the (hyper-)nucleus. In Tab. I, we list the measured rms of the wave-function, λ_A^{meas}, as well as the r_A parameter derived according to these relations. We encourage future more rigorous numerical studies that address the calculation of coalescence probabilities with more realistic wave-functions, e.g. the Hulthen parameterisation for the deuteron [6] or a Λ-deuteron parameterisation for the hyper-triton as done for central collisions in [42]. The difference between such calculations and our predictions would also indicate the uncertainty associated with the coalescence model.

The quantum-mechanical nature of the coalescence products is explicitly accounted for by means of an average quantum-mechanical correction factor, $\langle C_A \rangle$. In the case of the deuteron, the quantum-mechanical correction factor $\langle C_d \rangle$ has been approximated as

$$\langle C_d \rangle \approx \frac{1}{\left[1+\left(\frac{r_d}{2R_\perp(m_T)}\right)^2\right]\sqrt{1+\left(\frac{r_d}{2R_\parallel(m_T)}\right)^2}} \tag{4}$$

where r_d is the radius of the deuteron, $R_\perp$ and $R_\parallel$ are the lengths of homogeneity of the coalescence volume and

m_T is the transverse mass of the coalescing nucleons. The size of the nucleus enters in the determination of the coalescence parameter B_2 via $\langle C_d \rangle$, as well as the homogeneity volume $R_\perp^2 R_\parallel$, according to the relation

$$B_2 = \frac{3\pi^{3/2}\langle C_d \rangle}{2m_T R_\perp^2(m_T)R_\parallel(m_T)} \tag{5}$$

which is the main result of [7]. It is interesting to note that the coalescence parameter decreases with increasing volume, as expected. In addition to this, the quantum-mechanical correction factor introduces a length scale defined by the deuteron size relative to the source size in the calculation of B_2, which reflects the coalescence probability. If we assume that $R_\perp \approx R_\parallel \approx R$, Eqs. 4 and 5 simplify to

$$\langle C_d \rangle \approx \left[1+\left(\frac{r_d}{2R(m_T)}\right)^2\right]^{-3/2} \tag{6}$$

and

$$B_2 = \frac{3\pi^{3/2}\langle C_d \rangle}{2m_T R^3(m_T)}. \tag{7}$$

Figure 1 shows the source radius (R) dependence of the quantum-mechanical correction factor (on the left) and the coalescence parameter B_2 (on the right), calculated assuming (a.) a point-like nucleus $r_d = 0$, (b.) $r_d = 0.3$ fm, (c.) the actual value which reproduces the measured rms radius of the deuteron $r_d = 3.2$ fm [24], (d.) a larger, irrealistic value of $r_d = 10$ fm. As can be seen in Fig. 1, the quantum-mechanical correction factor leads to a significant suppression in the production of those objects whose radius is large compared to that of the source. As a matter of fact, the inflection point of $\langle C_d \rangle$ is situated at $R = r_d/\sqrt{6}$, as indicated in the left panel of Fig. 1 by the vertical dotted line for $r_d = 3.2$ fm.

Following the approach and discussion presented in [9], Eq. 4 may be generalised as

$$\langle C_A \rangle = \prod_{i=1,2,3}\left(1+\frac{r^2}{4R_i^2}\right)^{-\frac{1}{2}(A-1)} \tag{8}$$

for mass number A and the radii R_i that describe the volume of the emitting source. Similarly, the coalescence parameter B_A for a nucleus with mass number A and spin J_A is generalised by Eq. 6.2 in [7]. In particular, for the case of ^{3}He with $A = 3$ and $J = 1/2$, the latter becomes the Eq. 9 presented in [9].

In summary, under the assumption $R_1 \approx R_2 \approx R_3 \approx R$ as in [9] (see details in next section) and by combining Eq. 6.2 in [7] and Eq. 8, we obtain the following general expression for the coalescence parameter:

$$B_A = \frac{2J_A+1}{2^A}\frac{1}{\sqrt{A}}\frac{1}{m_T^{A-1}}\left(\frac{2\pi}{R^2+(\frac{r_A}{2})^2}\right)^{3/2(A-1)} . \tag{9}$$
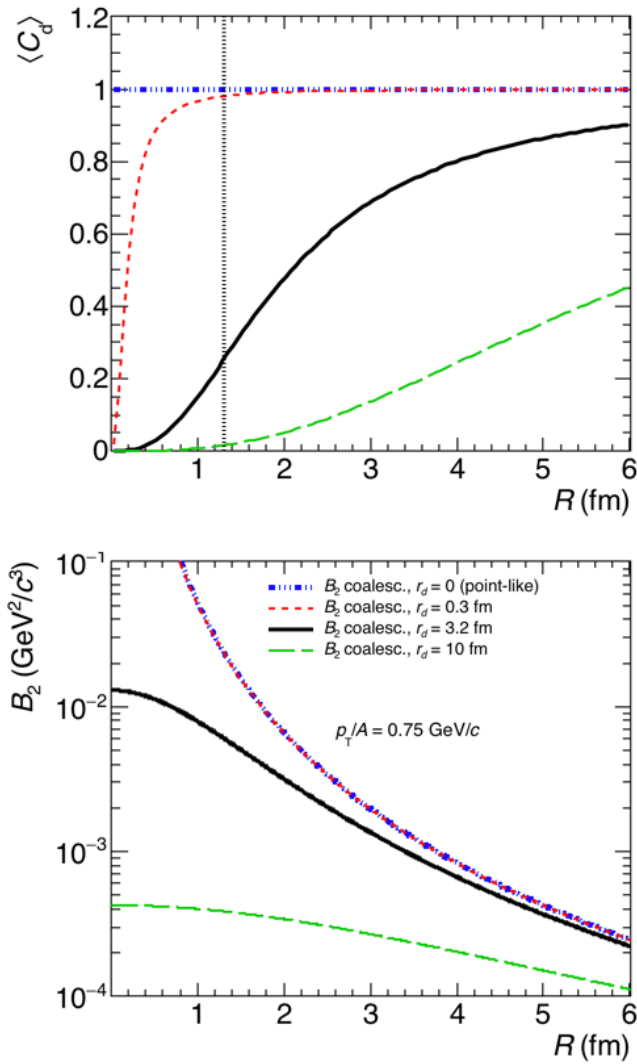
FIG. 1. The quantum-mechanical correction factor $\langle C_d \rangle$ (left panel, see Eq. 6) and the coalescence parameter B_2 for deuteron (right panel, see Eq. 7) as a function of the radius of the source R, calculated assuming a size parameter for the deuteron $r_d = 0, 0.3, 3.2$ and 10 fm. The inflection point of $\langle C_d \rangle$ corresponds to $R = r_d/\sqrt{6}$ and is indicated in the left panel by the vertical dotted line for $r_d = 3.2$ fm.

This formula can be used to compare the predicted B_A with experimental data directly.

We understand the relation between B_A and the radii as follows: for small radii of the source, as $R \to 0$, the coalescence probability appears to be anti-proportional to the harmonic oscillator size parameter r_A, and thus proportional to the depth of the attractive potential in the harmonic oscillator picture (and thus to the nucleus binding energy). Quite naturally, the allowed momentum difference between the coalescing nucleons is larger for more attractive, i.e. deeper, potentials. For large source volume, i.e. $R \gg r_A$, the coalescence probabil-

ity is dominated by the classical phase-space separation, and thus decreases for large differences in configuration space.

A. Source volume

We identify the source volume as the effective sub-volume of the whole system that is governed by the homogeneity length of the interacting nucleons, as in [7]. The latter is much smaller that the entire fireball which is created in heavy-ion collisions. This is not only caused by the limitations ascribed to the causally-connected volume, but also to the presence of a common radial expansion, which causes the particles inside the fireball to be sorted according to their velocities. As pointed out by the same authors, this volume is experimentally accessible with Hanbury-Brown-Twiss (HBT) interferometry. The experimental results are typically obtained following the Bertsch-Pratt (BP) parameterisation $(R_{out}, R_{side}, R_{long})$, while the coalescence model described in Section II expresses the volume in terms of the Yano-Koonin-Podgoretskii (YKP) parameterisation. As discussed in Appendix A, we identify $R_\perp = R_{side}$ and $R_\parallel = R_{long}$. We then take $R = (R_\perp^2 R_\parallel)^{1/3} \approx (R_{side}^2 R_{long})^{1/3}$.

Experimentally, the size of the effective volume can be controlled by selecting different collision geometries, i.e. different centrality classes [43]. In heavy-ion collisions the HBT radii are known to scale with the cubic root of the average charged particle multiplicity density $\langle dN_{ch}/d\eta \rangle^{1/3}$ [1], and to depend on the pair average transverse momentum $\langle k_T \rangle$ [44]. In the following, we make the simplifying assumption that the scaling with $\langle dN_{ch}/d\eta \rangle^{1/3}$ holds across collision systems, which is approximately fulfilled in data [45]. In contrast to [9], we therefore do not explicitly use the measured HBT radii in our study, but we derive the radii from the measured $\langle dN_{ch}/d\eta \rangle$ according to the following relation:

$$R = a \langle dN_{ch}/d\eta \rangle^{1/3} + b . \tag{10}$$

The coefficients, $a = 0.339$ and $b = 0.128$ (in units of fm), have been determined by fitting linearly the ALICE data, and the parameterisation is reported in Fig. 2. The values we obtain by interpolating the geometric mean of the measured radii are consistent with the radii from kaon femtoscopy for $m_T \approx 1$ GeV/c in low-multiplicity pp collisions [46] and the radii from pion femtoscopy in high-multiplicity Pb–Pb collisions at the highest available $k_T \approx 0.9$ GeV/c [1]. The highest k_T bin was chosen as it is closest in m_T to the lowest transverse momentum per nucleon ($p_T/A \approx 0.8$ GeV/c) accessible by ALICE for the measurement of nuclei production. Ideally, one would use the proton femtoscopic radii for such a study, but given that these measurements are not available in all collision systems and centralities, we assume that m_T-scaling holds for HBT radii [47]. We acknowledge that

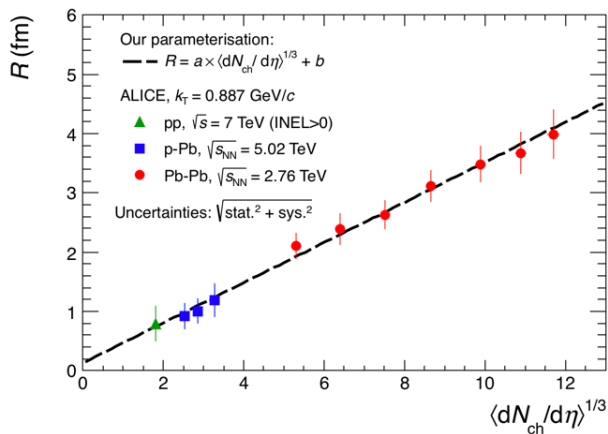a model-based scaling factor is proposed by [48], which alternatively could be considered.

FIG. 2. Parameterisation of the dependence of the source radius on multiplicity assumed in this paper, compared to HBT data from [1, 45, 46]. The radius R and the parameters a and b are in units of fm. Parameterisation A is shown here, see text for details.

III. STATISTICAL-THERMAL APPROACH AND BLAST-WAVE

In the statistical-thermal approach, the yields $(\mathrm{d}N/\mathrm{d}y)$ of light anti- and hyper-nuclei are very sensitive to the chemical freeze-out temperature T_{chem} due to their large mass m and approximately scale as $\mathrm{d}N/\mathrm{d}y \propto \exp(-m/T_{chem})$. As a matter of fact, the chemical freeze-out temperature defines the only scale in this model, since at the LHC the chemical potentials which ensure the conservation of baryon number (μ_B), strangeness (μ_S), and electric charge (μ_Q) are negligible. In contrast to the coalescence approach, the statistical-thermal model [49–51] provides only p_{T}-integrated yields. Therefore, p_{T} spectra have been modelled using a blast-wave [52] parameterization. When extracting the predicted spectrum for a given particle species (proton, Λ, deuteron, ^{3}He), the parameters of the blast-wave (average radial flow velocity $\langle\beta_T\rangle$, kinetic freeze-out temperature T_{kin}, and velocity profile n) are fixed to the values obtained from the simultaneous fit to the pion, kaon and proton spectra measured in Pb–Pb collisions as a function of centrality by ALICE [16]. The normalisation is fixed using the p_{T}-integrated deuteron-to-pion ratio and ^{3}He-to-pion ratio predicted by the GSI-Heidelberg model with $T_{chem} = 156$ MeV, multiplied by the pion yield measured by ALICE [16]. This choice, as opposed to using the ratio to proton, is motivated by the fact that the measured proton yield is seen to be slightly overestimated by the thermal model predictions at the LHC [53]. In the case of hyper-triton, a slightly different procedure is chosen,

namely the normalisation for $^3_\Lambda$H is extracted from the statistical-thermal model prediction of the strangeness population factor $S_3 = \frac{^3_\Lambda H/^3 \mathrm{He}}{\Lambda/p}$ multiplied by the measured Λ/p ratio [16, 54] and the measured ^{3}He yield [40]. Based on the spectra obtained in this way, we calculate the corresponding coalescence parameters for a given p_{T}/A and compare it with coalescence expectations. Because we use experimental data to constrain the blast-wave prediction as well as the normalisation, and because such data are provided for given centrality classes, we use the corresponding $\langle\mathrm{d}N_{\mathrm{ch}}/\mathrm{d}\eta\rangle$ in each class to estimate the system radius based on the parameterisation discussed in Sec. II A. Whereas the coalescence approach explicitly depends on the size of the produced object with respect to the system size, the object size does not enter in the formulation of the blast-wave model. The thermal model on the other hand, implements eigenvolume corrections by fixing the object radius as an external parameter (0.3 fm for baryons in the GSI-Heidelberg model [12]). We refer to the literature for the extensive discussions on the validity of the eigenvolume correction for light (anti-)(hyper-)nuclei [55] and the relation with the possible production of these objects as compact quark bags [12].

IV. COMPARISON WITH EXPERIMENTAL DATA

A. Constraining the source volume with data

Data on anti- and hyper-nuclei production at LHC energies and different collision systems have been released by the ALICE Collaboration in recent years [20, 37, 39, 40]. In Fig. 3 we compare the coalescence parameter for deuteron (B_2) from the coalescence model (see Eqs. 5 and 7, with $r_d = 3.2$ fm) to the ALICE data for Pb-Pb collisions at $\sqrt{s_{\mathrm{NN}}} = 2.76$ TeV and pp collisions at $\sqrt{s} = 7$ TeV. For pp collisions, data in [37] are given for inelastic (INEL) collisions. In order to facilitate the comparison with future multiplicity-dependent data given in the INEL>0 class, we have rescaled the B_2 and B_3 by the ratio of the charged particle multiplicity density in these two event classes [56]. First, the parameterisation of the system radius fitted to the HBT data as described in Sec. II A (labeled in the following as "parameterisation A") is used to map the $\langle\mathrm{d}N_{\mathrm{ch}}/\mathrm{d}\eta\rangle$ to the source size (top left panel of Fig. 3). We notice already at this point that the coalescence volume from parameterisation A leads to discrepancies with respect to the curve from the coalescence calculation, and in particular, we notice that the model would require a larger radius for a given value of B_2 for Pb-Pb collisions.

In a second step the radius is tuned such that the data points for (anti-)deuterons fall onto the coalescence prediction (top right panel of Fig. 3). We find that the parameters of Eq. 10 turn out to be $a = 0.473$ and $b = 0$.

With this second parameterisation (labeled as "B" in the following), we investigate the agreement of the model with the measured coalescence parameter for ^{3}He, B_3. As shown in the lower panels of Fig. 3, also in the case of B_3, a tension between the model and the data is found for parameterisation A, which ameliorates for the parameterisation B, tuned to the (anti-)deuteron data. The strength of this approach is given by the fact that the coalescence volume is constrained with the more differential (anti-)deuteron data assuming that the coalescence volume is the same for all anti- and hyper-nuclei. It is also noteworthy that any change of the radii parameterisation would result in a shift along the x-axis of both B_2 and B_3 data points in the same way, while the theoretical coalescence curve would not be affected.

The necessity of introducing a second parameterisation for the radius could point to the fact that the kinetic freeze-out volume relevant for coalescence is not given by the m_T-scaled pion HBT volume considered in parameterisation A, but by a slightly larger system as given by parameterisation B.

B. Thermal and coalescence model for $A = 2, 3$ anti- and hyper-nuclei

In Fig. 4, the available data for (anti-)deuterons, (anti-)^{3}He and (anti-)$^3_\Lambda$H [39] are compared to coalescence and to the thermal model+blast wave predictions described in Sec. III. For the latter and for data, the radius parameterisation B is used, as discussed in Sec. IV A.

For deuterons, both approaches lead to similar predictions and give a reasonable description of the experimental data for $R \gtrsim 1.6$ fm. For ^{3}He the two models exhibit a qualitatively similar trend as a function of R, but they differ by a factor of about 1.5 to 2. The limited amount of data that is currently available is consistent with both models within 2σ to 3σ, where σ is the total uncertainty on the data. Both approaches show large differences (a factor 5 to 6 for central Pb–Pb collisions and a factor larger than 50 for small radii, $R < 2$ fm) for the $^3_\Lambda$H caused by the significantly larger size of $^3_\Lambda$H with respect to ^{3}He. The only data point available so far in Pb–Pb collisions is in agreement with the thermal model but not with coalescence. The difference between data and the coalescence model is about 6σ, albeit the validity of our assumptions (*in primis* the usage of a gaussian wave-function). In [42] it is argued that the difference between data and the coalescence model might be explained by a later formation through the coalescence of Λs and deuterons. A possible difference attributable to the presence of excited states with $J = 3/2$ of $^3_\Lambda$H, which would significantly enhance the phase space for its production, is not considered here as there is no evidence for the existence of such an excited state [57].

Most importantly, Fig. 4 shows that the difference between the two approaches increases with decreasing source volume, thus underlining the need for additional and more precise data as a function of multiplicity or centrality in order to distinguish between the two production scenarios. In the case of $^3_\Lambda$H we have considered also a prediction from coalescence for a wider wave-function (dashed line in bottom right panel of Fig. 4), which results in even lower production probabilities. This behaviour highlights the unique potential to constrain the wave-function of the particle under study at the moment of its production via precise measurements of the coalescence parameter as a function of the source volume. The curves presented here also explicitly allow for an estimate of the expected hyper-triton production in pp collisions. As it can be seen, the latter is expected to be suppressed by about two orders of magnitude with respect to the production of ^{3}He, thus making this measurement a prime candidate for future experimental studies.

V. CONCLUSIONS AND OUTLOOK

We summarise our main conclusions as follows:

1. For the production of $A = 2$ and $A = 3$ (anti-)nuclei in heavy-ion collisions, the thermal and coalescence models give similar predictions for a source volume that is constrained by experimental data on d, $\bar{\text{d}}$ production in central Pb–Pb collisions at the LHC.

2. For the production of hyper-triton, the thermal and coalescence models give very different predictions as a function of source volume. In particular, the yield of hyper-triton appears to be suppressed by about two orders of magnitude in pp collisions with respect to the production of ^{3}He. The very limited amount of currently available data favours the thermal model prediction within our assumptions.

3. Systematic measurements in pp, p–Pb, and Pb–Pb collisions at LHC energies have a unique potential to clarify the production mechanism and the nature of composite QCD objects. Ideally, such measurements are accompanied by systematic measurements of the HBT radii in the same multiplicity/centrality classes and collision systems.

As our study is deliberately based on simplified assumptions that allow for a completely analytical treatment of the problem, future studies should be based on more realistic approximations (in particular the wave-function), which require numerical calculations. Moreover, it will be interesting to explore further the p_T dependence of the observations made here in comparison to future and currently available data.

In a follow-up publication, we plan to extend our study to predictions for the $A = 4$ systems introduced in Tab. I and to more exotic QCD objects like the X(3872), which has been interpreted as tetraquark state or hadronic molecule [8, 35]. In fact, if the X(3872) corresponds to
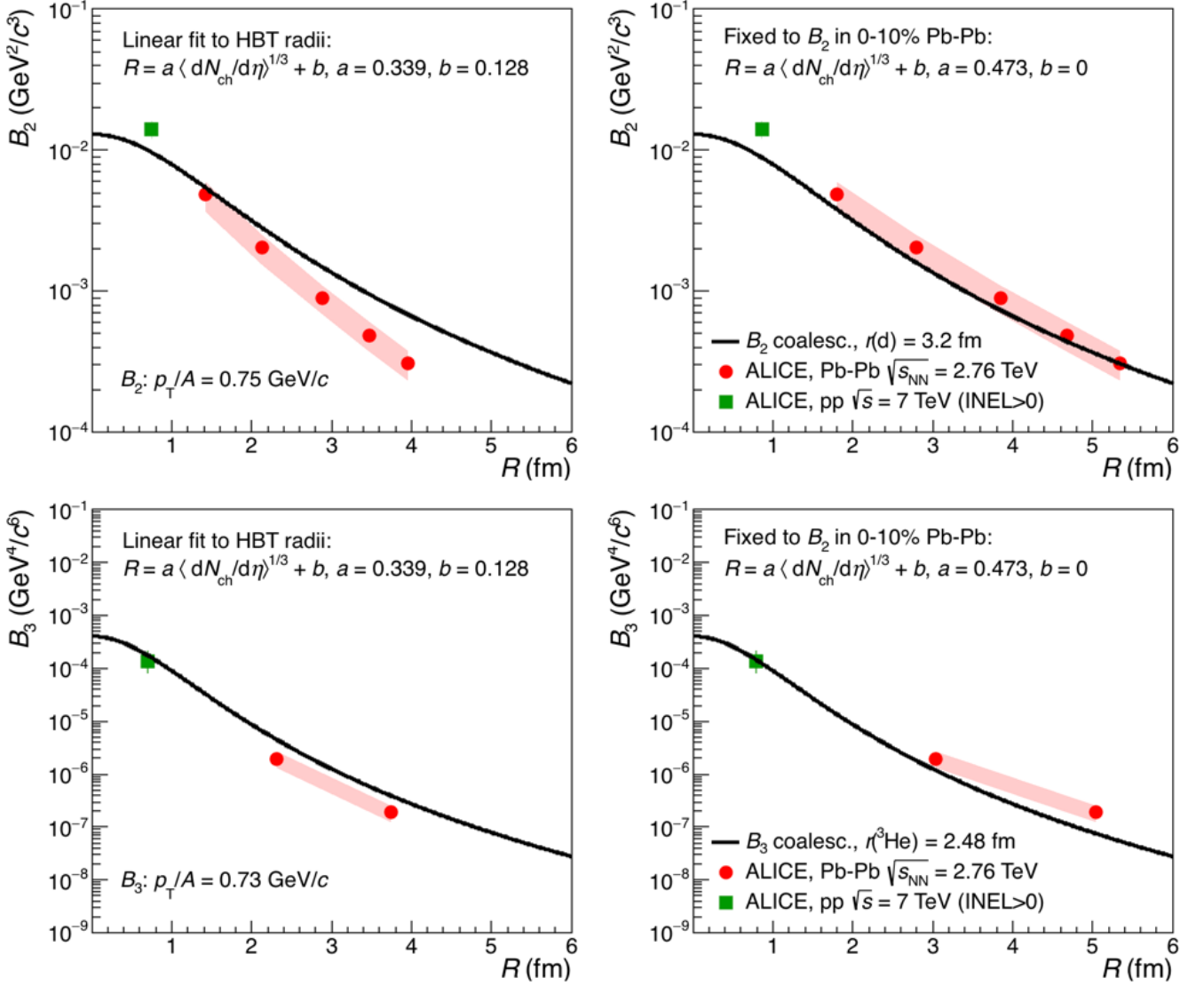
FIG. 3. Comparison of the ALICE data from [37, 40] with the coalescence prediction for two different mappings of the $\langle dN_{ch}/d\eta \rangle$ to the system size R: (left panels) the parameterisation A, fitted to the HBT radii, (right panels) the parameterisation B, tuned to the B_2 values in central Pb-Pb collisions. The radius R and the parameters a and b are in units of fm.

a loosely bound $\overline{D}^{*0}$–D^0 molecule, the rms of its wavefunction can be as large as $4.9^{+13.4}_{-1.4}$ fm [58], which is very similar to that of the hyper-triton. Thus, its possible production via a coalescence mechanism in pp collisions would be subject to a similar suppression as the hypertriton. The upcoming high-luminosity phase of the LHC (Run 3 & 4), where $A = 4$ hyper-nuclei and other rare composite objects will become experimentally accessible, will provide a unique opportunity for the final understanding of (anti-)(hyper-)nuclei production. Setting a final word on the production mechanisms is not only in the interest of the heavy-ion community, but has a broader application in astrophysics and dark-matter searches, by representing an essential input for the measurement of (anti-)nuclei in space with ongoing [31, 32] and future
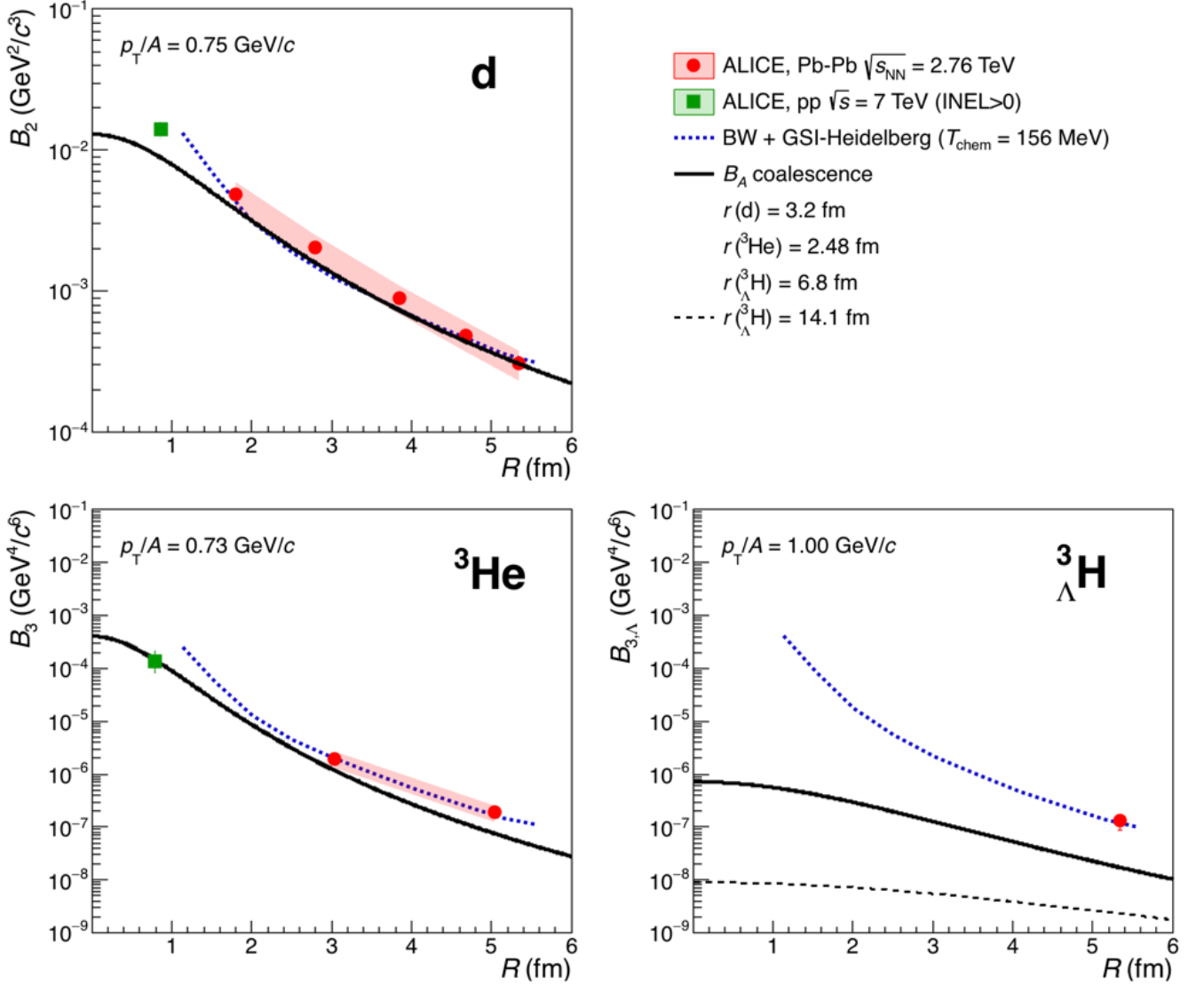
[33, 34] experiments.

FIG. 4. Comparison of the coalescence parameters measured by ALICE (solid markers) for deuterons (upper left panel), ^{3}He (lower left panel) and $^3_\Lambda$H (lower right panel) in pp [37] and Pb–Pb [39, 40] collisions with the thermal+blast-wave model expectations (dotted line) and the coalescence predictions (solid lines). Parameterisation B has been used to map the charged particle multiplicity density into the radius R of the source (see text for details). The dashed line in the lower right panel corresponds to the coalescence prediction for the $^3_\Lambda$H with a larger radius.

the ALICE Collaboration for their valuable input.

Appendix A: Relation to the Sato-Yazaki coalescence model

The approach of Sato and Yazaki [5] is based on a density matrix model and includes explicitly the system size dependence and wave-function dependence of the coalescence process albeit it assumes a sudden approximation when particles cease their interactions (sudden freeze-out) and thus neglects the collective expansion of the medium in contrast to [7]. It assumes no correlation between different nucleons and no correlation between coordinates in space and momentum. In a heavy ion collisions, such correlations are consequence of hydrodynamical flow. The coalescence process to form a nucleus with mass number $A = Z + N$ is formulated in terms of the momentum per nucleon (p) as

$$\frac{\gamma_A}{\sigma_{A,0}}\frac{d^3\sigma_A}{d^3p} = \left(\frac{4}{3}\pi p_0^3\right)^{A-1}\frac{1}{Z!N!}\left(\frac{\gamma_p}{\sigma_{p,0}}\frac{d^3\sigma_p}{d^3p_p}\right)^Z\left(\frac{\gamma_n}{\sigma_{n,0}}\frac{d^3\sigma_n}{d^3p_n}\right)^N \tag{A1}$$

where p_0 corresponds to the coalescence momentum, γ_A and $\gamma_{p,n}$ are the Lorentz factors for the nucleus and the nucleons, respectively. The reaction cross-sections are

denoted as $\sigma_{i,0}$, where $A = p, n, A$. Assuming that the proton and neutron emission probabilities are equal and that $p_p \approx p_n \equiv p$, this expression relates to the B_A as defined by our Lorentz invariant Eq.(1) as

$$B_A = \left(\frac{4}{3}\pi p_0^3\right)^{A-1} \frac{M}{m^A} \frac{1}{A^3} \frac{1}{Z!N!} \tag{A2}$$

where the factor $\frac{1}{A^3}$ results from the transformation of $p_A \to A p_{p,n}$ and M corresponds to the nucleus mass and m to the nucleon mass. This expression can be further simplified via the approximation $M \approx Am$ to

$$B_A = \left(\frac{4}{3}\pi p_0^3\right)^{A-1} \frac{1}{m^{A-1}} \frac{1}{A^2} \frac{1}{Z!N!} \ . \tag{A3}$$

For nuclei up to $A = 4$ and the non-relativistic case, Sato and Yazaki derive the following relations for the coalescence momentum p_0,

$$A = 2 \qquad \frac{4}{3}\pi p_0^3 = \frac{3}{4} 2^{3/2} (4\pi)^{3/2} \left(\frac{\nu_2 \nu}{\nu_2 + \nu}\right)^{3/2} \tag{A4}$$

$$A = 3 \quad \frac{1}{2}\left(\frac{4}{3}\pi p_0^3\right)^2 = \frac{1}{4} 3^{3/2} (4\pi)^3 \left(\frac{\nu_3 \nu}{\nu_3 + \nu}\right)^3 \tag{A5}$$

$$A = 4 \quad \frac{1}{4}\left(\frac{4}{3}\pi p_0^3\right)^3 = \frac{1}{16} 4^{3/2} (4\pi)^{9/2} \left(\frac{\nu_4 \nu}{\nu_4 + \nu}\right)^{9/2} \tag{A6}$$

where the size parameter ν relates to the rms radius R_{rms} of the emission source as $\nu = \sqrt{\frac{3}{2R_{rms}}}$, and ν_A is the size parameter of the nucleus.
Following the generalisation in [6], we thus propose the following parameterisation for the coalescence parameter

$$B_A = \frac{2J_A + 1}{2^A} A^{3/2} (4\pi)^{\frac{3}{2}(A-1)} \left(\frac{\nu_A \nu}{\nu_A + \nu}\right)^{\frac{3}{2}(A-1)} \frac{1}{m^{A-1}} \frac{1}{A^2} \tag{A7}$$

$$= \frac{2J_A + 1}{2^A} \frac{1}{m^{A-1}} \frac{1}{\sqrt{A}} (4\pi)^{\frac{3}{2}(A-1)} \left(\frac{\nu_A \nu}{\nu_A + \nu}\right)^{\frac{3}{2}(A-1)} \tag{A8}$$

indicating with J_A the spin of the nucleus. Once again, the ν_A parameter corresponds to the size parameter of the nucleus wave-function, which is assumed to be gaussian (solution to the isotropic spherical harmonic oscillator potential) of the form [5, 59]:

$$\phi_A = C \exp\left(-\frac{1}{2}\nu_A \sum_{i=1}^{A} (\vec{x}_i - \vec{X})^2\right) \tag{A9}$$

with an appropriate normalisation factor C and the coordinate vector $\vec{X}$ of the centre-of-mass system.

We have also verified that our generalisation of Sato-Yazaki provided by Eq. A8 and the expression derived from Heinz in Eq. 8 become consistent in the limit

$R_{rms} \approx R \to 0$ (point-like source) and $p_T \to 0$ (static source), provided that one identifies $\nu_A = 2/r_A^2$. Incidentally, the same relation between ν_A and r_A can be derived by a straightforward comparison of the nucleus wave-functions employed by the same authors [5, 7].

The parameter ν_A is typically chosen such that the measured rms charge radius λ_A is reproduced. The relation between λ_A and ν_A is obtained by a transformation to the Jacobi variables and performing the integration (see Appendix A). In particular, one obtains for $A < 5$:

$$A = 2 \qquad \nu_2 = \frac{3}{4\lambda_2^2} \tag{A10}$$

$$A = 3 \qquad \nu_3 = \frac{1}{\lambda_3^2} \tag{A11}$$

$$A = 4 \qquad \nu_4 = \frac{9}{8\lambda_4^2} \ . \tag{A12}$$

Appendix A: RMS of a gaussian wave-function for A = 4

In this appendix, we show the calculation of the RMS of a gaussian wave-function with the example of $A = 4$. We start from the wave-function

$$\phi_{A=4} = C_4 \exp\left(-\frac{1}{2}\nu_4 \sum_{i=1}^{4} (\vec{x}_i - \vec{X})^2\right) \ . \tag{A1}$$

Then we introduce the Jacobi variables which are given by

$$\vec{X} = \frac{1}{4}(\vec{x_1} + \vec{x_2} + \vec{x_3} + \vec{x_4}) \tag{A2}$$

$$\vec{r_1} = \vec{x_2} - \vec{x_1} \tag{A3}$$

$$\vec{r_2} = \vec{x_3} - \frac{1}{2}(\vec{x_1} + \vec{x_2}) \tag{A4}$$

$$\vec{r_3} = \vec{x_4} - \frac{1}{3}(\vec{x_1} + \vec{x_2} + \vec{x_3}) \ . \tag{A5}$$

In this parameterisation we can express the squared distance of each nucleon with respect to the centre-of-mass as

$$\sum_{i=1}^{4} (\vec{x}_i - \vec{X})^2 = \frac{1}{4}\left(2\vec{r_1} + \frac{8}{3}\vec{r_2} + 3\vec{r_3}\right) \ . \tag{A6}$$

For the following integral calculations we determine the Jacobian as

$$\mathrm{d}R\mathrm{d}r_1\mathrm{d}r_2\mathrm{d}r_3 = |\det \frac{\partial(R, r_1, r_2, r_3)}{\partial(x_1, x_2, x_3, x_4)}| \, \mathrm{d}x_1\mathrm{d}x_2\mathrm{d}x_3\mathrm{d}x_4$$

$$(A7)$$

$$= \begin{vmatrix} \frac{\partial R}{\partial x_1} & \frac{\partial r_1}{\partial x_1} & \frac{\partial r_2}{\partial x_1} & \frac{\partial r_3}{\partial x_1} \\ \frac{\partial R}{\partial x_2} & \frac{\partial r_1}{\partial x_2} & \frac{\partial r_2}{\partial x_2} & \frac{\partial r_3}{\partial x_2} \\ \frac{\partial R}{\partial x_3} & \frac{\partial r_1}{\partial x_3} & \frac{\partial r_2}{\partial x_3} & \frac{\partial r_3}{\partial x_3} \\ \frac{\partial R}{\partial x_4} & \frac{\partial r_1}{\partial x_4} & \frac{\partial r_2}{\partial x_4} & \frac{\partial r_3}{\partial x_4} \end{vmatrix} \mathrm{d}x_1\mathrm{d}x_2\mathrm{d}x_3\mathrm{d}x_4$$

$$(A8)$$

$$= \begin{vmatrix} \frac{1}{4} & -1 & -\frac{1}{2} & -\frac{1}{3} \\ \frac{1}{4} & 1 & -\frac{1}{2} & -\frac{1}{3} \\ \frac{1}{4} & 0 & 1 & -\frac{1}{3} \\ \frac{1}{4} & 0 & 0 & 1 \end{vmatrix} \mathrm{d}x_1\mathrm{d}x_2\mathrm{d}x_3\mathrm{d}x_4 \quad (A9)$$

$$= 1 \cdot \mathrm{d}x_1\mathrm{d}x_2\mathrm{d}x_3\mathrm{d}x_4 \, . \qquad (A10)$$

From the requirement $\int |\phi|^2 \mathrm{d}\vec{r}_1\mathrm{d}\vec{r}_2\mathrm{d}\vec{r}_3 = 1$, we thus obtain for the normalisation constant C_4:

$$\frac{1}{C_4^2} = \int \exp^2\left(-\frac{1}{2}\nu_4\left(\frac{1}{2}r_1^2 + \frac{2}{3}r_2^2 + \frac{3}{4}r_3^2\right)\right)\mathrm{d}\vec{r}_1\mathrm{d}\vec{r}_2\mathrm{d}\vec{r}_3$$

$$(A11)$$

where the integration in spherical coordinates is performed with $\mathrm{d}\vec{r}_1 = 4\pi r_1^2 \mathrm{d}r_1, \mathrm{d}\vec{r}_2 = \dots$ which gives

$$\frac{1}{C_4^2} = (4\pi)^3 \underbrace{\int_0^\infty r_1^2 \exp\left(-\frac{1}{2}\nu_4 r_1^2\right)\mathrm{d}r_1}_{\frac{\sqrt{\pi}}{4}\frac{1}{(\frac{1}{2}\nu_4)^{3/2}}} \underbrace{\int_0^\infty r_2^2 \exp\left(-\frac{2}{3}\nu_4 r_2^2\right)\mathrm{d}r_2}_{\frac{\sqrt{\pi}}{4}\frac{1}{(\frac{2}{3}\nu_4)^{3/2}}} \underbrace{\int_0^\infty r_3^2 \exp\left(-\frac{3}{4}\nu_4 r_3^2\right)\mathrm{d}r_3}_{\frac{\sqrt{\pi}}{4}\frac{1}{(\frac{3}{4}\nu_4)^{3/2}}}$$

$$(A12)$$

$$= \left(\frac{\pi}{\nu_A}\right)^{9/2} 4^{3/2} \qquad (A13)$$

$$\Rightarrow C_4 = \left(\frac{\nu_A^3}{4\pi^3}\right)^{3/4} \, . \qquad (A14)$$

For the rms, we obtain accordingly:

$$\lambda_4^2 = \frac{1}{4}\langle\phi| \sum_{i=1}^4 (\vec{x}_i - \vec{X})^2 |\phi\rangle \qquad (A15)$$

$$= \int \frac{1}{4} \sum_{i=1}^4 (\vec{x}_i - \vec{X})^2 |\phi|^2 \mathrm{d}\vec{x}_1\mathrm{d}\vec{x}_2\mathrm{d}\vec{x}_3\mathrm{d}\vec{x}_4 \qquad (A16)$$

$$= \frac{C_4^2}{4} \int \left(\frac{1}{2}r_1^2 + \frac{2}{3}r_2^2 + \frac{3}{4}r_3^2\right) \exp^2\left(-\frac{1}{2}\nu_4\left(\frac{1}{2}r_1^2 + \frac{2}{3}r_2^2 + \frac{3}{4}r_3^2\right)\right)\mathrm{d}\vec{r}_1\mathrm{d}$$

$$(A17)$$

$$= \frac{C_4^2}{4}\Big(\underbrace{\frac{1}{2}\int r_1^2 \exp\left(-\frac{1}{2}\nu_A r_1^2\right)\exp\left(-\frac{2}{3}\nu_A r_2^2\right)\exp\left(-\frac{3}{4}\nu_A r_3^2\right)\mathrm{d}\vec{r}_1\mathrm{d}\vec{r}_2\mathrm{d}}_{\mathrm{I}}$$

$$(A18)$$

$$+ \underbrace{\frac{2}{3}\int r_2^2 \exp\left(-\frac{1}{2}\nu_A r_1^2\right)\exp\left(-\frac{2}{3}\nu_A r_2^2\right)\exp\left(-\frac{3}{4}\nu_A r_3^2\right)\mathrm{d}\vec{r}_1\mathrm{d}\vec{r}_2\mathrm{d}\vec{r}_3}_{\mathrm{II}}$$

$$(A19)$$

$$+ \underbrace{\frac{3}{4}\int r_3^2 \exp\left(-\frac{1}{2}\nu_A r_1^2\right)\exp\left(-\frac{2}{3}\nu_A r_2^2\right)\exp\left(-\frac{3}{4}\nu_A r_3^2\right)\mathrm{d}\vec{r}_1\mathrm{d}\vec{r}_2\mathrm{d}\vec{r}_3}_{\mathrm{III}}\Big)$$

$$(A20)$$

The first summand I can be calculated with $\mathrm{d}\vec{r}_1\mathrm{d}\vec{r}_2\mathrm{d}\vec{r}_3 = (4\pi)^3 r_1^2 r_2^2 r_3^2 \mathrm{d}r_1\mathrm{d}r_2\mathrm{d}r_3$ as

$$\mathrm{I} = \frac{1}{2}(4\pi)^3 \cdot \int_0^\infty r_1^2 \exp\left(-\frac{1}{2}\nu_A r_1^2\right)\mathrm{d}r_1 \cdot \int_0^\infty \exp\left(-\frac{2}{3}\nu_A r_2^2\right)\mathrm{d}r_2 \cdot \int_0^\infty \mathrm{ex}$$

$$(A21)$$

$$= \frac{1}{2}(4\pi)^3 \cdot \frac{3\sqrt{\pi}}{8}\frac{1}{(\frac{1}{2}\nu_A)^{5/2}} \cdot \frac{\sqrt{\pi}}{4}\frac{1}{(\frac{2}{3}\nu_A)^{3/2}} \cdot \frac{\sqrt{\pi}}{4}\frac{1}{(\frac{3}{4}\nu_A)^{3/2}} \cdot$$

$$(A22)$$

The other two summands II and III are evaluated accordingly and we thus obtain for the rms:

$$\lambda_4^2 = \frac{C_4^2}{4}(\mathrm{I} + \mathrm{II} + \mathrm{III}) \qquad (A23)$$

$$= \frac{C_4^2}{4}(4\pi)^3 \frac{3\pi^{3/2}}{8 \cdot \nu_A^{11/2}}\underbrace{\Big(\frac{\frac{1}{2}}{(\frac{1}{2})^{5/2}(\frac{2}{3})^{3/2}(\frac{3}{4})^{3/2}} + \frac{\frac{2}{3}}{(\frac{1}{2})^{3/2}(\frac{2}{3})^{5/2}(\frac{3}{4})^{3/2}} + \dots}_{=24}$$

$$(A24)$$

$$= \frac{9}{8\nu_A} \, . \qquad (A25)$$

Appendix A: HBT radii in Bertsch-Pratt and Yano-Koonin-Podgoretskii parameterisation for comparison with coalescence models

The results of HBT analyses are typically presented in either the Bertsch-Pratt ($R_{out}, R_{side}, R_{long}$) or the

Yano-Koonin-Podgoretskii ($R_\perp$, R_0, $R_\parallel$) parameterization. The ALICE HBT results [1, 44] are given in the Bertsch-Pratt convention, whereas the coalescence parameter is derived in [7] by expressing the dependence on the volume in terms of the Yano-Koonin-Podgoretskii (YKP) parameterisation. The transformation between the two parameterisations is best presented in [60] in the equations (W 3.48) to (W 3.52)[61]:

$$R_{side}^2 = R_\perp^2 \,, \tag{A1}$$

$$R_{diff}^2 = R_{out}^2 - R_{side}^2 = \beta_\perp^2 \gamma^2 (R_0^2 + v^2 R_\parallel^2) \,, \tag{A2}$$

$$R_{long}^2 = (1 - \beta_l^2)R_\parallel^2 + \gamma^2(\beta_l - v)^2(R_0^2 + v^2 R_\parallel^2) \,, \tag{A3}$$

$$R_{ol}^2 = \beta_\perp(-\beta_l R_\parallel^2 + \gamma^2(\beta_l - v)(R_0^2 + v^2 R_\parallel^2)) \,. \tag{A4}$$

We immediately identify that $R_\perp^2$ can be identified with R_{side}^2. Following the reasoning and the nomenclature in [60] (W 3.52-3.53), the above equations can be inverted and $R_\parallel^2$ can be expressed as

$$R_\parallel^2 = B - v \cdot C \,, \tag{A5}$$

$$= R_{long}^2 - 2\frac{\beta_l}{\beta_\perp}R_{ol}^2 + \frac{\beta_l^2}{\beta_\perp^2}R_{diff}^2 - v \cdot \left(-\frac{1}{\beta_\perp}R_{ol}^2 + \frac{\beta_l}{\beta_\perp^2}R_{diff}^2\right) \tag{A6}$$

As it turns out all corrections which are subtracted from R_{long}^2 can be neglected. First, we notice that the cross term R_{ol} vanishes if the measured fireball is longitudinally boost-invariant, which is a valid approximation for the rapidity ranges studied here. The remaining terms are all proportional to β_l. By definition of the rest frame for a longitudinally-boosted invariant system, $\beta_l = 0$. In summary, we can consider $R_\perp = R_{side}$ and $R_\parallel = R_{long}$ for the present study.

[1] J. Adam *et al.* (ALICE), Phys. Rev. **C93**, 024905 (2016), arXiv:1507.06842 [nucl-ex].
[2] H. Nemura, Y. Suzuki, Y. Fujiwara, and C. Nakamoto, Prog. Theor. Phys. **103**, 929 (2000), arXiv:nucl-th/9912065 [nucl-th].
[3] S. T. Butler and C. A. Pearson, Phys. Rev. **129**, 836 (1963).
[4] J. I. Kapusta, Phys. Rev. **C21**, 1301 (1980).
[5] H. Sato and K. Yazaki, Phys. Lett. **B98**, 153 (1981).
[6] J. L. Nagle, B. S. Kumar, D. Kusnezov, H. Sorge, and R. Mattiello, Phys. Rev. **C53**, 367 (1996).
[7] R. Scheibl and U. W. Heinz, Phys. Rev. **C59**, 1585 (1999), arXiv:nucl-th/9809092 [nucl-th].
[8] S. Cho *et al.* (ExHIC), Prog. Part. Nucl. Phys. **95**, 279 (2017), arXiv:1702.00486 [nucl-th].
[9] K. Blum, K. C. Y. Ng, R. Sato, and M. Takimoto, Phys. Rev. **D96**, 103021 (2017), arXiv:1704.05431 [astro-ph.HE].
[10] S. Bazak and S. Mrowczynski, (2018), arXiv:1802.08212 [nucl-th].
[11] W. Zhao, L. Zhu, H. Zheng, C. M. Ko, and H. Song, (2018), arXiv:1807.02813 [nucl-th].
[12] A. Andronic, P. Braun-Munzinger, K. Redlich, and J. Stachel, (2017), arXiv:1710.09425 [nucl-th].
[13] A. Andronic, P. Braun-Munzinger, J. Stachel, and H. Stocker, Physics Letters B **697**, 203 (2011).
[14] A. Bazavov *et al.* (HotQCD), Phys. Rev. **D90**, 094503 (2014), arXiv:1407.6387 [hep-lat].
[15] R. Bellwied, S. Borsanyi, Z. Fodor, S. D. Katz, and C. Ratti, Phys. Rev. Lett. **111**, 202302 (2013), arXiv:1305.6297 [hep-lat].
[16] B. Abelev *et al.* (ALICE), Phys. Rev. **C88**, 044910 (2013), arXiv:1303.0737 [hep-ex].
[17] H. Garcilazo, Phys. Rev. Lett. **48**, 577 (1982).
[18] S. A. Bass *et al.*, Prog. Part. Nucl. Phys. **41**, 255 (1998), arXiv:nucl-th/9803035 [nucl-th].
[19] J. Schukraft, *Proceedings, 26th International Conference on Ultra-relativistic Nucleus-Nucleus Collisions (Quark Matter 2017): Chicago, Illinois, USA, February 5-11, 2017*, Nucl. Phys. **A967**, 1 (2017), arXiv:1705.02646 [hep-ex].
[20] S. Acharya *et al.* (ALICE), Eur. Phys. J. **C77**, 658 (2017), arXiv:1707.07304 [nucl-ex].
[21] U. Heinz, "Coalescence model involving HBT and flow," Presentation at EMMI Workshop in Torino, November 2017.
[22] B. B. Abelev *et al.* (ALICE), Phys. Rev. **C91**, 024609 (2015), arXiv:1404.0495 [nucl-ex].
[23] C. Van Der Leun and C. Alderliesten, Nucl. Phys. **A380**, 261 (1982).
[24] P. J. Mohr, D. B. Newell, and B. N. Taylor, Rev. Mod. Phys. **88**, 035009 (2016), arXiv:1507.07956 [physics.atom-ph].
[25] J. E. Purcell and C. G. Sheu, Nucl. Data Sheets **130**, 1 (2015).
[26] D. H. Davis, *Proceedings on 8th International Conference on Hypernuclear and strange particle physics (HYP 2003): Newport News, USA, October 14-18, 2003*, Nucl. Phys. **A754**, 3 (2005).
[27] M. Wang, G. Audi, F. Kondev, W. Huang, S. Naimi, and X. Xu, Chinese Physics C **41**, 030003 (2017).
[28] I. Angeli and K. P. Marinova, Atom. Data Nucl. Data Tabl. **99**, 69 (2013).
[29] J. C. Bernauer *et al.* (A1), Phys. Rev. Lett. **105**, 242001 (2010).
[30] S. Mrowczynski, Acta Phys. Polon. **B48**, 707 (2017), arXiv:1607.02267 [nucl-th].
[31] J. Alcaraz *et al.* (AMS), Phys. Lett. **B461**, 387 (1999), arXiv:hep-ex/0002048 [hep-ex].
[32] V. Poulin, P. Salati, I. Cholis, M. Kamionkowski, and J. Silk, (2018), arXiv:1808.08961 [astro-ph.HE].
[33] S. Schael, "AMS-100 - A Magnetic Spectrometer at Lagrange Point 2," Presentation at AMS days La Palma, April 2018.
[34] T. Aramaki, C. J. Hailey, S. E. Boggs, P. von Doetinchem, H. Fuke, S. I. Mognet, R. A. Ong, K. Perez, and J. Zweerink (GAPS), Astropart. Phys. **74**, 6 (2016), arXiv:1506.02513 [astro-ph.HE].
[35] A. Esposito, A. L. Guerrieri, L. Maiani, F. Piccinini, A. Pilloni, A. D. Polosa, and V. Riquer, Phys. Rev.

D92, 034028 (2015), arXiv:1508.00295 [hep-ph].

[36] E. Abbas *et al.* (ALICE), Eur. Phys. J. **C73**, 2496 (2013), arXiv:1305.1562 [nucl-ex].

[37] S. Acharya *et al.* (ALICE), Phys. Rev. **C97**, 024615 (2018), arXiv:1709.08522 [nucl-ex].

[38] Anielski, Jonas, *Proceedings, Hot Quarks 2014: Workshop for young scientists on the physics of ultrarelativistic nucleus–nucleus collisions, Andalucia, Spain*, J. Phys. Conf. Ser. **612**, 012014 (2015).

[39] J. Adam *et al.* (ALICE), Phys. Lett. **B754**, 360 (2016), arXiv:1506.08453 [nucl-ex].

[40] J. Adam *et al.* (ALICE), Phys. Rev. **C93**, 024917 (2016), arXiv:1506.08951 [nucl-ex].

[41] A. Shebeko, P. Papakonstantinou, and E. Mavrommatis, Eur. Phys. J. **A27**, 143 (2006), arXiv:nucl-th/0602056 [nucl-th].

[42] Z. Zhang and C. M. Ko, Phys. Lett. **B780**, 191 (2018).

[43] B. Abelev *et al.* (ALICE), Phys. Rev. **C88**, 044909 (2013), arXiv:1301.4361 [nucl-ex].

[44] K. Aamodt *et al.* (ALICE), Phys. Lett. **B696**, 328 (2011), arXiv:1012.4035 [nucl-ex].

[45] J. Adam *et al.* (ALICE), Phys. Rev. **C91**, 034906 (2015), arXiv:1502.00559 [nucl-ex].

[46] B. Abelev *et al.* (ALICE), Phys. Rev. **D87**, 052016 (2013), arXiv:1212.5958 [hep-ex].

[47] J. Adam *et al.* (ALICE), Phys. Rev. **C92**, 054908 (2015), arXiv:1506.07884 [nucl-ex].

[48] A. Kisiel, M. Ga?a?yn, and P. Bo?ek, Phys. Rev. **C90**, 064914 (2014), arXiv:1409.4571 [nucl-th].

[49] M. Petran, J. Letessier, J. Rafelski, and G. Torrieri, Comput. Phys. Commun. **185**, 2056 (2014), arXiv:1310.5108 [hep-ph].

[50] S. Wheaton and J. Cleymans, Comput. Phys. Commun. **180**, 84 (2009), arXiv:hep-ph/0407174 [hep-ph].

[51] A. Andronic, P. Braun-Munzinger, and J. Stachel, Nucl. Phys. **A772**, 167 (2006), arXiv:nucl-th/0511071 [nucl-th].

[52] E. Schnedermann, J. Sollfrank, and U. W. Heinz, Phys. Rev. **C48**, 2462 (1993), arXiv:nucl-th/9307020 [nucl-th].

[53] B. Abelev *et al.* (ALICE), Phys. Rev. Lett. **109**, 252301 (2012), arXiv:1208.1974 [hep-ex].

[54] B. B. Abelev *et al.* (ALICE), Phys. Rev. Lett. **111**, 222301 (2013), arXiv:1307.5530 [nucl-ex].

[55] V. Vovchenko and H. Stoecker, *Proceedings, 16th International Conference on Strangeness in Quark Matter (SQM 2016): Berkeley, California, United States*, J. Phys. Conf. Ser. **779**, 012078 (2017), arXiv:1610.02346 [nucl-th].

[56] J. Adam *et al.* (ALICE), Eur. Phys. J. **C77**, 33 (2017), arXiv:1509.07541 [nucl-ex].

[57] T. Mart, L. Tiator, D. Drechsel, and C. Bennhold, Nucl. Phys. **A640**, 235 (1998), arXiv:nucl-th/9610038 [nucl-th].

[58] P. Artoisenet and E. Braaten, Phys. Rev. **D83**, 014019 (2011), arXiv:1007.2868 [hep-ph].

[59] J. C. Bergstrom, Nucl. Phys. **A327**, 458 (1979).

[60] U. A. Wiedemann and U. W. Heinz, Phys. Rept. **319**, 145 (1999), arXiv:nucl-th/9901094 [nucl-th].

[61] The equations in [60] are denoted as (W...) in order to distinguish them from the equations presented in this paper.